Exploration of Ultra-High Current Operation in PEFC Using a Validated Model

L. Zheng[a], A. K. Srouji[a], F. Gambini[b], M. M. Mench[c]

[a] Department of Mechanical and Nuclear Engineering, The Pennsylvania State University, University Park, PA 16801, USA
[b] Nuvera Fuel Cells Inc., Billerica, MA 01821, USA
[c] Electrochemical Energy Storage and Conversion Laboratory, Department of Mechanical, Aerospace and Biomedical Engineering, University of Tennessee, Knoxville, TN 37996, USA

A comprehensive 2D+1 mathematical model has been developed to explore the operation of a polymer electrolyte fuel cell (PEFC) in the ultra-high current density regime ($>2A/cm^2$). The accuracy of this model has been partially validated with simultaneous in-situ experimental testing in terms of performance, high frequency resistance (HFR) and net water drag coefficient. The experimental and modeling investigation found that for the unique open flow field architecture used, gas phase mass transport is not the limiting factor even in ultra-high current regime.

Introduction

Among the potential hydrogen-based energy conversion devices, the polymer electrolyte fuel cell (PEFC) has been through intense development. The most recent advances in the materials and design of PEFC have enabled stable operation at a current density greater than $2A/cm^2$. The achievement of high current density, however, comes with unprecedented challenges in heat and water management. This ultra-high current regime has been largely unexplored in the scientific literature to date from either the experimental or modeling perspective.

The dimensionality of the computational PEFC models has been advancing in the last two decades, from one-dimensional simulations which focused almost exclusively on the through-plane direction, to the two-dimensional domain which accounted for an additional in-plane or along-the-channel direction, to fully-solved three-dimensional models (1-5). These additional dimensions made possible the study of the land-channel cell architecture, the varying composition along the channel and many other associated effects. The higher-dimensional models obviously require greater computational resources, however. A pseudo 3D, or 2D+1 model, which fully solves the through-plane and in-plane direction while simplifying the solution in the along-channel dimension, is a compromise between the computational cost and accuracy.

The degree of complexity in treating liquid water has progressed as well, from the early single-phase models which considered only gas phase transport, to the truly two-phase model which considered gas-liquid interaction, to the transient model which considered non-equilibrium phase transfer (6, 7). Considering the amount of heat and

product water, a rigorous non-isothermal and two-phase model is needed to describe the physics of phase-change-induced (PCI) flow (8).

Although the thinnest in the fuel cell assembly, the catalyst layer is undoubtedly the most complicated layer to model in that transport of ions, electrons, heat and mass and electro-chemical reaction take place. To better describe the sluggish oxygen reduction reaction (ORR), reflect the flooding effects, and enable optimization of structural parameters in the catalyst layer, agglomerate catalyst layer models combine the porous electrode with an additional agglomerate length-scale. Most of the current agglomerate models are cathode-only half-cell models though, unable to simulate the important water balance at high current density (9-12).

To tackle the critical issue of water and heat management, a full-cell computational model is necessary, which should include all anode and cathode layers to capture water transport across the membrane, account for three geometric dimensions of the cell, solve the cathode catalyst layer with the rigorous agglomerate model and consider the non-isothermal effects and PCI flow. In the following sections, the experimental setup and the development of such a comprehensive model are detailed. The Results and Discussion section is focused on the model validation and transport study with heliox.

Experimental Setup

A 50 cm^2 single cell open flow field (SCOF or OME) designed by Nuvera Fuel Cells Inc. was used in this study. Coolant water passed outside the flow fields in order to keep the outer boundaries of the cell at the desired temperature at coolant inlet. The membrane electrode assembly (MEA) used in the testing shown here was W. L. Gore and Associates Inc. Primea® series 57 with 0.4 and 0.15 mg/cm^2 Pt loading at the cathode and anode, respectively. The dry membrane thickness was 18 μm. The carbon paper diffusion media (DM) with micro-porous layer (MPL) used for both electrodes was Sigracet SGL 25 BC.

An fuel cell test station designed by Arbin Instruments controlled the gas flow rates and the electronic load. A Nafion® type humidifier system from Fuel Cell Technologies Inc. controlled the reactants' dew points. The HFR was monitored with a milliohmmeter from Agilent Technologies Inc. Back pressure was controlled with a back pressure module by Scribner Associates Inc.

Performance curves were reduced by taking the 45 minutes average potential response of each operating point in galvanostatic mode. Unless otherwise specified, a protocol labeled "automotive conditions" was used. Automotive conditions consisted of the cell operating temperature of 60°C, a hydrogen dew point of 47°C at the anode, and dry breathing grade air at the cathode. The anode stoichiometry was set to 2 throughout all current density. As current density increased from 0.125 to 3 A/cm^2, cathode stoichiometry increased from 1.6 to 2. Both anode and cathode back pressure was set to equal value and throttled from 1.70 to 11.60 psig. The heliox test consisted of using a mixture of helium and oxygen at the cathode (21% oxygen, bal. helium), and all else the same.

To compute the net water drag coefficient, two RH sensors by Vaisala were used after precisely calibrated, one at the cathode outlet and another at the anode outlet. Outlet lines

and sensors were heated in order to avoid water condensation and moist flow before reaching the humidity sensors.

Model Development

The computational domain of the 2D+1 model as shown in Figure 1(a) is the polymer-electrolyte membrane (PEM) sandwiched by catalyst layer (CL), micro-porous layer (MPL), macro-porous diffusion media (DM) and open metallic element (OME) on both sides. The 2D+1 model is differentiated from a full three-dimensional model by not solving the along-channel direction, designated as y axis in Figure 1(a), to its full extent. Instead the information in y direction is passed from the x-z control volumes to the adjacent ones through the changes in boundaries conditions of the 2D sub-model. In the limit of sufficiently fine discretization, this 2D+1 model becomes full 3D.
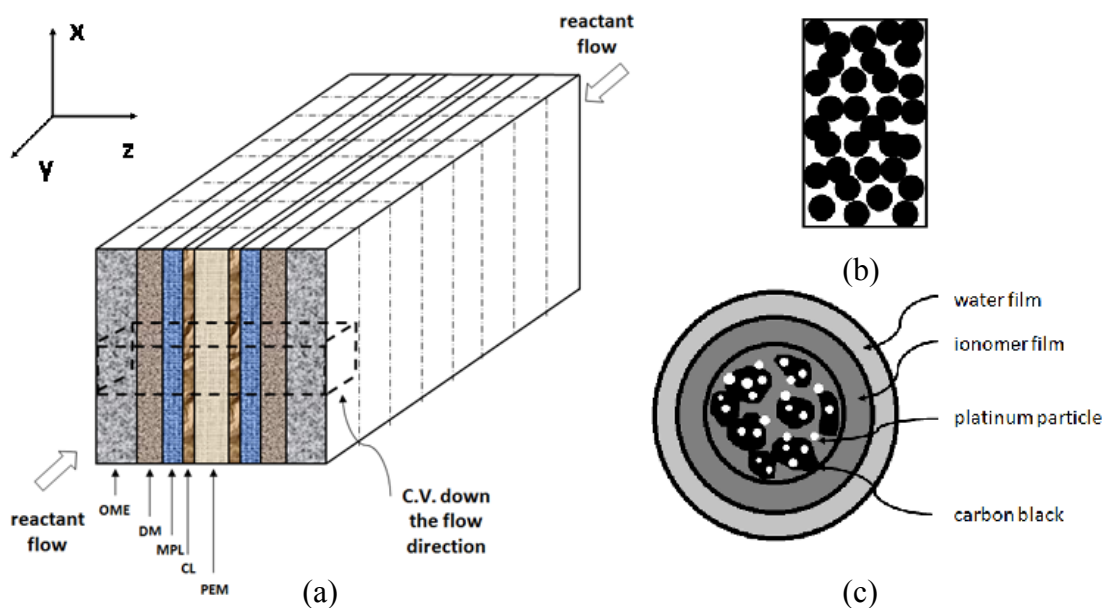

Figure 1. Schematics of (a) three-dimensional computational domain, (b) catalyst layer and (c) spherical agglomerate particle.

Assumptions

- The cell reaches steady-state operation.
- The product water of the electro-chemical reaction is in liquid form and then phase change process such as evaporation and condensation occurs until phase equilibrium is achieved.
- Material properties are homogeneous within individual layer, but can be anisotropic.
- Knudsen diffusion is considered only in micro-porous layer and catalyst layer considering the pore size. Knudsen diffusion and bulk diffusion are treated as resistance in series.
- The agglomerate in the catalyst layer is an isothermal and equipotential spherical. The ORR is a first-order reaction.
- The water dissolved into the ionomer phase is calculated by the equilibrium water sorption.

Governing Equations and Boundary Conditions for 2-D Sub-model

The governing equations of mass, heat and charge transport in the through-plane and in-plane directions for the 2-D sub-model are summarized in Table I.

Table I Governing Equations

	OME DM MPL	CL	PEM
C_{O_2}	$\nabla\cdot(\bar{N}_{O_2,conv})+\nabla\cdot(\bar{N}_{O_2,diff})=0$	$\nabla\cdot(\bar{N}_{O_2,conv})+\nabla\cdot(\bar{N}_{O_2,diff})=-\dfrac{J_{gen}}{4F}$	/
C_{H_2}	$\nabla\cdot(\bar{N}_{H_2,conv})+\nabla\cdot(\bar{N}_{H_2,diff})=0$	$\nabla\cdot(\bar{N}_{H_2,conv})+\nabla\cdot(\bar{N}_{H_2,diff})=-\dfrac{J_{gen}}{2F}$	/
C_{H_2O}	$\nabla\cdot(\bar{N}_{H_2O,conv})+\nabla\cdot(\bar{N}_{H_2O,diff})=-S_{vl}$	$\nabla\cdot(\bar{N}_{H_2O,conv})+\nabla\cdot(\bar{N}_{H_2O,diff})=-S_{vl}$	/
C_d	/	$\nabla\cdot(-D_d\nabla C_d)=-\nabla\cdot\left(\dfrac{n_d}{F}\bar{i}\right)+\dfrac{J_{gen}}{2F}$	$\nabla\cdot(-D_d\nabla C_d)=-\nabla\cdot\left(\dfrac{n_d}{F}\bar{i}\right)$
T	$\nabla\cdot(\rho C_p\bar{u}T)+\nabla\cdot(-k\nabla T)=\overline{H_{vl}}S_{vl}$	$\nabla\cdot(\rho C_p\bar{u}T)+\nabla\cdot(-k\nabla T)=-J_{gen}(\eta+\dfrac{T\Delta S}{nF})+\dfrac{i^2}{\kappa}+\overline{H_{vl}}S_{vl}$	$\nabla\cdot(-k\nabla T)=+\dfrac{i^2}{\kappa}$
P_G	$\nabla\cdot\left(-C_T\dfrac{K_G}{\mu_G}\nabla P_G\right)=-S_{vl}$	$\nabla\cdot\left(-C_T\dfrac{K_G}{\mu_G}\nabla P_G\right)=-\dfrac{J_{gen}}{nF}-S_{vl}$	/
P_L	$\nabla\cdot\left(-\dfrac{\varepsilon_0 s\rho_w}{M_w}\dfrac{K_L}{\mu_L}\nabla P_L\right)=S_{vl}$	$\nabla\cdot\left(-\dfrac{\varepsilon_0 s\rho_w}{M_w}\dfrac{K_L}{\mu_L}\nabla P_L\right)=S_{vl}$	$\nabla\cdot\left(-\dfrac{\rho_w}{M_w}\dfrac{K_L}{\mu_L}\nabla P_L\right)=0$
φ_e	/	$\nabla\cdot(-\kappa\nabla\varphi_e)=-J_{gen}$	$\nabla\cdot(-\kappa\nabla\varphi_e)=0$
φ_s	$\nabla\cdot(-\sigma\nabla\varphi_s)=0$	$\nabla\cdot(-\sigma\nabla\varphi_s)=J_{gen}$	/

In the porous media, the convective mass flux $\bar{N}_{i,conv}$ can be written as

$$\bar{N}_{i,conv}=\bar{u}_G C_i \qquad [1]$$

where $\bar{u}_G$ is the gas phase velocity, and C_i is the concentration of species i.

Stefan-Maxwell multi-species diffusion is applied to the ternary system in the cathode side components, so that the diffusive mass flux $\bar{N}_{i,diff}$ can be expressed as

$$\nabla x_i=\sum_{j\neq i}\frac{x_i\bar{N}_{j,diff}-x_j\bar{N}_{i,diff}}{c_T D_{i,j}^{eff}} \qquad [2]$$

where x_i is the mole fraction of species i and c_T is the total concentration of all species. $D_{i,j}^{eff}$ is the effective binary diffusion coefficient between species i and j, which has been corrected by the Bruggeman relation in the porous media and Knudsen diffusion for pore size effect.

The physical phenomenon of phase change is described by the source or sink term,

$$S_{vl}=k_{vl}\left(C_{H2O}RT-P_{sat}\right) \qquad [3]$$

where k_{vl} is the mass transfer coefficient between vapor and liquid phase and P_{sat} is the vapor saturation pressure.

By the equilibrium sorption approach, the concentration of dissolved phase water C_d is empirically correlated to water content in the membrane λ in the following way

$$C_d = \frac{\rho_{dry}}{EW}\lambda \qquad\qquad [4]$$

where ρ_{dry} is the density of dry membrane and EW is the equivalent molecular weight of the dry membrane.

The boundary conditions used in the 2-D sub-model are illustrated in Figure 2 and Table II.
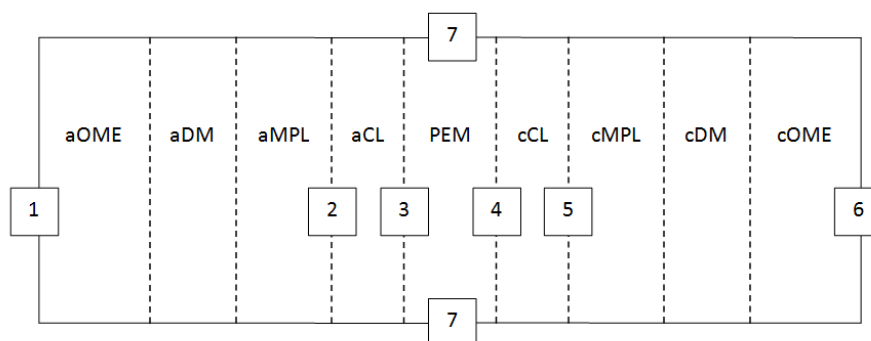

Figure 2. Boundary types of the 2-D computational domain

Table II Boundary Conditions

	1 z=0	2 z=aMPL|aCL	3 z=aCL|PEM	4 z=PEM|cCL	5 z=cCL|cMPL	6 z=L	7 x=0&x=W
C_{O_2}	/	/	/	$\frac{\partial C_{O_2}}{\partial z}=0$	/	$C_{O_2}=C_{O_2}^{specified}$	$\frac{\partial C_{O_2}}{\partial x}=0$
C_{H_2}	$C_{H_2}=C_{H_2}^{specified}$	/	$\frac{\partial C_{H_2O}}{\partial z}=0$	/	/	/	$\frac{\partial C_{H_2}}{\partial x}=0$
C_{H_2O}	$C_{H_2O}=C_{H_2O}^{specified}$	/	/	/	/	$C_{H_2O}=C_{H_2O}^{specified}$	$\frac{\partial C_{H_2O}}{\partial x}=0$
T	$T=T^{specified}$	/	/	/	/	$T=T^{specified}$	$\frac{\partial T}{\partial x}=0$
P_G	$p_G=p_G^{specified}$	/	/	/	/	$p_G=p_G^{specified}$	$\frac{\partial p_G}{\partial x}=0$
P_L	$p_L=p_L^{specified}$	/	/	/	/	$p_L=p_L^{specified}$	$\frac{\partial p_L}{\partial x}=0$
φ_e	/	$\frac{\partial \varphi_e}{\partial z}=0$	/	/	$\frac{\partial \varphi_e}{\partial z}=0$	/	$\frac{\partial \varphi_e}{\partial x}=0$
φ_s	$\varphi_s=\varphi^{specified}$	/	/	/	/	$\varphi_s=0$	$\frac{\partial \varphi_s}{\partial x}=0$

Catalyst Layer Agglomerate Model

As observed in a scanning electron microscope (SEM) study of the catalyst layer structure, there are agglomerates covered by ionomer and possibly water thin film on top of that in addition to the gas voids in the catalyst layer (13). Within the agglomerate, the catalyst platinum particles are dispersed on the carbon black and ionomer fills out the space in-between, the ideal scenario of which are shown in Figure 1(b) and (c). In order for the ORR to proceed, the oxygen must transport through the pores in catalyst layer, dissolve into the water or ionomer thin film covering the spherical agglomerate and diffuse until reaching the catalyst.

The transfer current density, J_{gen}, resulting from the agglomerate catalyst layer model can be written as

$$J_{gen} = 4F\left(\frac{C_{O_2}}{H_N}\right)^{\gamma_c}\left[\frac{1}{\left(1-\varepsilon_0^{CL}\right)E_r k_c} + \frac{H_W}{H_N}\cdot\frac{\delta_W}{a_{agg}D_{O_2,W}}\cdot\frac{r_{agg}+\delta_N}{r_{agg}+\delta_N+\delta_W} + \frac{\delta_N}{a_{agg}D_{O_2,N}}\cdot\frac{r_{agg}+\delta_N}{r_{agg}}\right]^{-1}(1-s) \quad [5]$$

where H_N and H_W are the dimensionless Henry's constant values of oxygen dissolved into ionomer and water thin film respectively, δ_N and δ_W are the thickness of ionomer and water thin film respectively and $D_{O_2,N}$ and $D_{O_2,W}$ are diffusion coefficient of oxygen in ionomer and water respectively. The radius of the idealized spherical agglomerate is r_{agg} and the effective surface area to dissolve oxygen into agglomerate is a_{agg}.

The reaction rate constant k_c in Equation [5], is written as

$$k_c = \frac{ai_{0,c}^{ref}}{4FC_{O_2,ref}^{\gamma_c}}\exp\left(-\frac{\alpha_{c,c}F}{R_u T}\eta\right) \quad [6]$$

where a is the roughness factor per unit volume, $i_{0,c}^{ref}$ is the reference exchange current density and $C_{O_2,ref}$ is the reference oxygen concentration.

The effective factor E_r of the reaction is

$$E_r = \frac{1}{\phi_L}\left(\frac{1}{\tanh(3\phi_L)} - \frac{1}{3\phi_L}\right) \quad [7]$$

where ϕ_L is the Thiele modulus for the ORR.

$$\phi_L = \frac{r_{agg}}{3}\sqrt{\frac{k_c}{D_{O_2,agg}^{eff}}} \quad [8]$$

Here $D_{O_2,agg}^{eff}$ is the effective diffusion coefficient of oxygen inside the agglomerate, written as

$$D_{O_2,agg}^{eff} = D_{O_2,N} \left(\varepsilon_{agg} \right)^{1.5} \qquad\qquad [9]$$

where ε_{agg} is the volume fraction of ionomer inside the agglomerate.

In contrast to the sluggish ORR in the cathode catalyst layer, the HOR in the anode catalyst layer is facile and can be formulated by Butler-Volmer kinetics as

$$J_{gen} = ai_{0,a}^{ref} (1-s) \left(\frac{C_{H_2}}{C_{H_2,ref}} \right)^{\gamma_a} \left[\exp\left(\frac{\alpha_{a,a}F}{R_uT}\eta \right) - \exp\left(\frac{-\alpha_{c,a}F}{R_uT}\eta \right) \right] \qquad [10]$$

Along-the-channel Conservation

At the respective inlet, the molar flow rate of reactants can be calculated

$$n_i = \xi_i \frac{iA}{nF} \qquad\qquad [11]$$

where ξ_i is the stoichiometry of species i.

The mass conservation for each species and heat conservation with coolant are guaranteed in the following way

$$n_{H_2}^{k+1} = n_{H_2}^{k} \mp \frac{i^k A'}{2F} \qquad\qquad [12]$$

$$n_{O_2}^{k+1} = n_{O_2}^{k} \mp \frac{i^k A'}{4F} \qquad\qquad [13]$$

$$n_{H_2O,a}^{k+1} = n_{H_2O,a}^{k} \mp \alpha^k \frac{i^k A'}{F} \qquad\qquad [14]$$

$$n_{H_2O,c}^{k+1} = n_{H_2O,c}^{k} \pm \left(\alpha^k + 0.5 \right) \frac{i^k A'}{F} \qquad\qquad [15]$$

$$T^{k+1} = T^k \pm \frac{i^k A'}{\dot{m}C_p} \left(V_{th} - V_{cell} \right) \qquad\qquad [16]$$

where α is the net water drag coefficient, defined as net amount of water transported through membrane from anode to cathode per proton. Whether plus or minus sign should be taken depends on whether the sweeping direction is with or against the flow direction. In this way the 2D+1 model is applicable to both co-current and counter-current configuration.

Results and Discussion

Experimental Operation in Ultra-High Current Regime

The experimental polarization curve shown in Figure 3 confirms that current density as high as $3A/cm^2$ can be achieved at the voltage of 0.40V with minimal relative mass-transport loss. Moreover, the power density peaks at around $3A/cm^2$, indicating that such high current density is not only a practical operating point for the single cell but also a desirable one from the stack point of view.
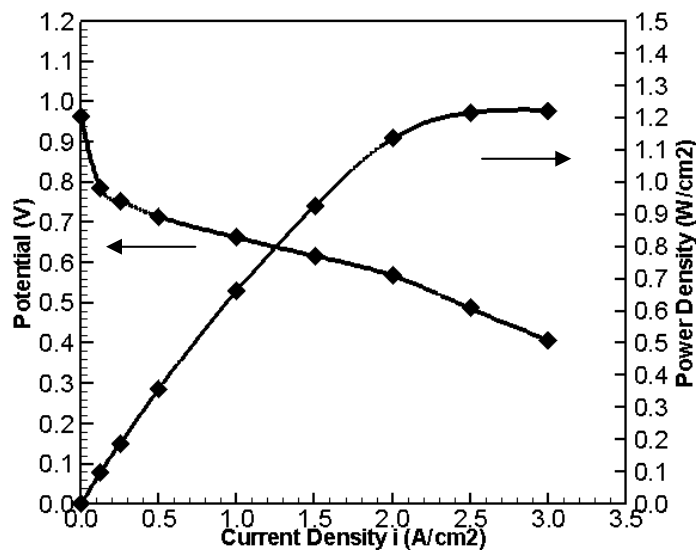

Figure 3. Voltage and power density under "automotive conditions" for the 50 cm^2 single cell with open metallic element

Model Validation

Under the "automotive conditions" same as in the testing, the predictions from 2D+1 mathematical model are compared with experimental results in Figure 4 in terms of performance and HFR with close agreement. Consistent with experimental results, the computational model predicts that the HFR increases with current density, which signifies the onset of the possible membrane dry-out in the ultra-high current density regime.
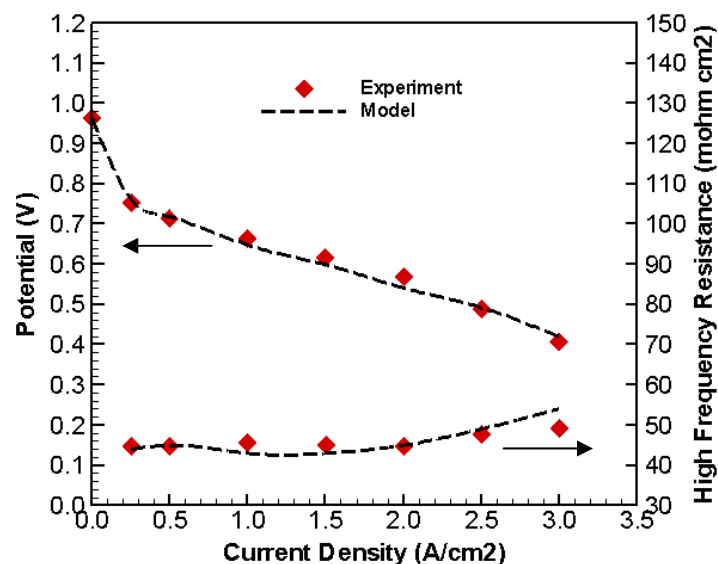
Figure 4. Comparison of voltage and HFR between experiment and model

To further validate the model, net water drag coefficient was measured as well. As observed from Figure 5, the overlap between the experimental and computational results is qualitatively achieved. Quantitatively, the net water drag coefficient at all current densities are slightly negative, except at low current densities. The negative net water drag coefficient means the net water transport through the membrane is from cathode to anode, which can be partially attributed to the MPL added in between the CL and DM. Considering the gas feed into the anode at medium relative humidity (RH≈52%) and into the cathode under dry conditions, the negative net drag coefficient is necessary to avoid dry-out, especially in the ultra-high current density regime. On the other hand, the possible flooding in the cathode components is alleviated by this negative net water drag coefficient. In all cases the optimal cell designs and operating conditions should keep the membrane and electrode hydrated while minimizing the flooding level.
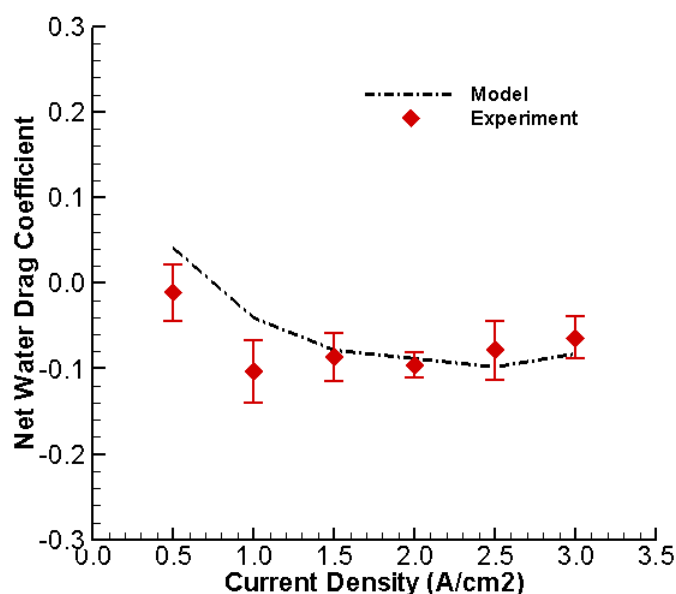

Figure 5. Comparison of net water drag coefficient between experiment and model

Mass Transport Study with Heliox

The mass transport can be studied by replacing the constituent of nitrogen in the air with helium. Since helium has a much smaller molecular weight than nitrogen, water vapor diffusion and oxygen diffusion in helium is about 2 times higher than that in nitrogen, as compared below. Therefore the multi-species diffusion process can be greatly facilitated in the ternary system on the cathode side, the phase-change-induced flow can be enhanced and the saturation level within the cell can be lowered through greater evaporation (14). This replacement usually improves mass transport, especially in heavily flooded cells where the difficulty of water vapor in moving out of the cell and oxygen in reaching the reaction site results in the limiting current density. This substitution with the SCOF cell, however, brings no benefit to the performance, as demonstrated by Figure 6. This implies that with this unique cell architecture the cell performance is not limited by concentration activation, even in ultra-high current regime, allowing stable operation at ultra-high current conditions.

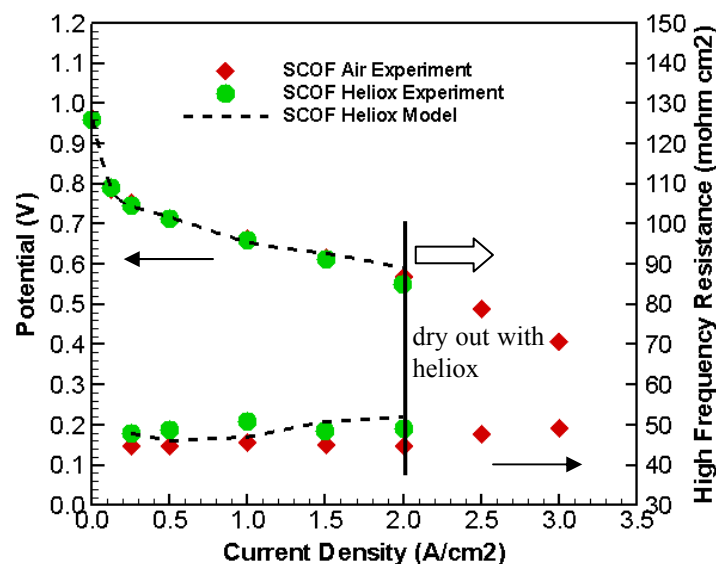| D_{O_2,N_2}	2.30×10^{-5} m^2/s	D_{H_2O,N_2}	2.93×10^{-5} m^2/s
$D_{O_2,He}$	8.22×10^{-5} m^2/s	$D_{H_2O,He}$	9.15×10^{-5} m^2/s

Figure 6. Comparison of voltage and HFR between air and heliox

Both modeling and experimental results show that the cell is not able to reach stable performance beyond 2.5A/cm^2 on heliox, due to dehydration of the anode. This phenomenon is a result of the enhanced water vapor removal from the cathode side. The HFR with heliox is not significantly higher than that with air, which can be explained as the HFR is the measurement of membrane hydration only, since electronic resistance in the catalyst layer can be orders of magnitude lower, especially considering reaction site for hydrogen oxidation reaction (HOR) is close to the membrane.

The predicted average water content in anode catalyst layer as a function of current is shown in Figure 7. This lower water content with heliox in anode catalyst layer can reduce the ion transport in the electrolyte as it dries. The fundamental reason for the lower water content with heliox can be found in the difference in net water drag coefficient shown in Figure 7. In comparison to the net water drag coefficient with air, which is close to but slightly below zero at high current density, the one with heliox is much more positive at higher current density, indicating dominance of electro-osmotic drag over back-diffusion. The side effect of facilitated gas transport and water vapor removal from cathode side is that the back diffusion is too weak to hydrate the anode side of membrane. In the extreme case where there is no water coming out of anode, indicated as "limit" in Figure 7, local dry-out occurs at the anode outlet, or cathode inlet.
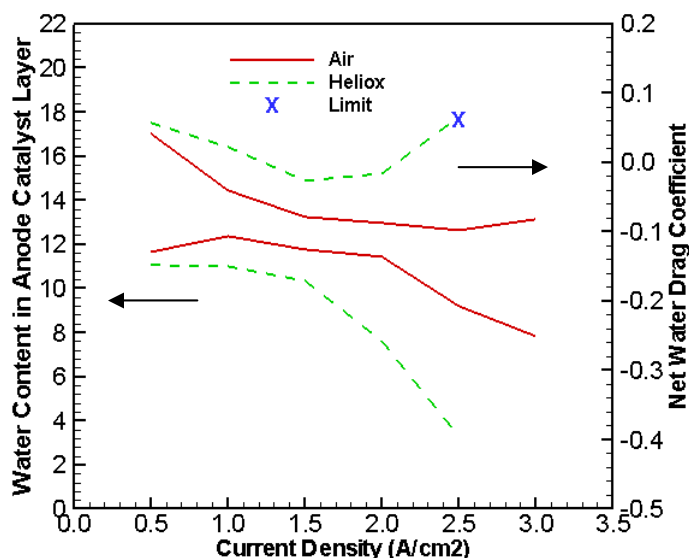

Figure 7. Comparison of net water drag coefficient and average water content in anode catalyst layer between air and heliox

Conclusion

In this paper, a comprehensive 2D+1 mathematical model is described which can simulate water balance through the membrane, capture the along-channel effects, resolve agglomerate length scale in the catalyst layer and reveal non-isothermal PCI effects at ultra-high current density. The validation of the model through performance, HFR and net water drag coefficient in the case of air and heliox shows its capability and accuracy. The study with heliox captures the anode dry-out phenomenon and shows the performance of the current cell in the high current regime is not limited by mass transport. Additional testing is underway to more completely validate this model and conduct parametric study on limiting feature at ultra-high current density.

Acknowledgments

References

1.   T. Springer, T. Zawodzinski, S. Gottesfeld, *J Electrochem Soc* **138**, 2334 (1991).
2.   D. Bernardi, M. Verbrugge, *J Electrochem Soc* **139**, 2477 (1992).
3.   W. He, J. Yi, T. Van Nguyen, *AIChE Journal* **46**, 2053 (2000).
4.   A. Weber, J. Newman, *J Electrochem Soc* **151**, A326 (2004).
5.   H. Meng, C. Wang, *J Electrochem Soc* **151**, A358 (2004).
6.   D. Natarajan, T. Van Nguyen, *J Electrochem Soc* **148**, A1324 (2001).
7.   H. Wu, P. Berg, X. Li, *Applied Energy* **87**, 2778 (2010).
8.   A. Weber, J. Newman, *J Electrochem Soc* **153**, A2205 (2006).
9.   D. Song *et al.*, *Electrochimica Acta* **50**, 3347 (2005).
10. W. Sun, B. Peppley, K. Karan, *Electrochimica Acta* **50**, 3359 (2005).
11. K. Yin, *J Electrochem Soc* **152**, A583 (2005).
12. M. Secanell, K. Karan, A. Suleman, N. Djilali, *Electrochimica Acta* **52**, 6318 (2007).
13. K. Broka, P. Ekdunge, *Journal of Applied Electrochemistry* **27**, 281 (1997).
14. K. T. Cho, M. M. Mench, *J Power Sources* **195**, 3858 (2010).